Originally published as:

Crustal surface wave velocity structure of the east Albany-Fraser Orogen, Western Australia, from ambient noise recordings

C. Sippl,[1,2] B.L.N. Kennett,[1] H. Tkalčić,[1] K. Gessner[3] and C.V. Spaggiari[3]

[1]*Research School of Earth Sciences, Australian National University, Canberra, Australia. E-mail: sippl@gfz-potsdam.de*
[2]*Section Lithosphere Dynamics, German Research Centre for Geosciences (GFZ), Potsdam, Germany*
[3]*Geological Survey of Western Australia, Perth, Australia*

SUMMARY

Group and phase velocity maps in the period range 2–20 s for the Proterozoic east Albany-Fraser Orogen, Western Australia, are extracted from ambient seismic noise recorded with the 70-station ALFREX array. This 2 yr temporary installation provided detailed coverage across the orogen and the edge of the Neoarchean Yilgarn Craton, a region where no passive seismic studies of this scale have occurred to date. The surface wave velocities are rather high overall (>3 km s^{-1} nearly everywhere), as expected for exposed Proterozoic basement rocks. No clear signature of the transition between Yilgarn Craton and Albany-Fraser Orogen is observed, but several strong anomalies corresponding to more local geological features were obtained. A prominent, NE-elongated high-velocity anomaly in the northern part of the array is coincident with a Bouguer gravity high caused by the upper crustal metamorphic rocks of the Fraser Zone. This feature disappears towards longer periods, which hints at an exclusively upper crustal origin for this anomaly. Further east, the limestones of the Cenozoic Eucla Basin are clearly imaged as a pronounced low-velocity zone at short periods, but the prevalence of low velocities to periods of ≥ 5 s implies that the uppermost basement in this area is likewise slow. At longer periods, slightly above-average surface wave velocities are imaged below the Eucla Basin.

Key words: Australia; Seismic tomography; Surface waves and free oscillations; Cratons; Crustal structure.

1 INTRODUCTION

The transition from Archean cratonic blocks to adjacent Proterozoic orogens usually has a clear signature in upper-mantle seismic velocities (e.g. Ritsema *et al.* 1998; Fishwick *et al.* 2005). Since the upper mantle is relatively homogeneous in terms of composition, seismic velocities are, to first order, determined by the temperature distribution. The mantle lithospheric keels that underlie cratons are colder than their surroundings, and therefore exhibit higher *P* and *S* wave speeds. Elevated shear wave speeds, usually gleaned from continent-wide studies of surface wave velocities, are thus frequently used to map out the lateral and depth extent of these keels (e.g. Kennett *et al.* 2013). At crustal depths, the distinction between Archean craton and Proterozoic orogen is significantly less straightforward, and global compilations of seismic wave speeds show no systematic difference between the two (Rudnick & Fountain 1995). The main reason for this observation is that the crustal seismic velocity field is primarily controlled by the heterogeneous lithology (e.g. Christensen & Mooney 1995), and not by temperature. However, there are cases where subtle systematic differences in crustal velocities between craton and adjacent orogen have been identified (e.g. Dalton *et al.* 2011).

In this study, we use ambient seismic noise recorded with a 70-station seismic array to image the upper and middle crustal surface wave velocity structure of the east Albany-Fraser Orogen (AFO), a Proterozoic orogen in southwestern Australia, and its transition to the adjacent Archean Yilgarn Craton. The deployment was designed to complement three active seismic profiles that were shot in 2012 near the northern and southern ends of the array (Fig. 1; Spaggiari *et al.* 2014b). An additional objective of this study is thus to check whether some of the seismic domains identified in the active seismic profiles possess a distinct signature in the surface wave velocities. We further interpret our results together with the regional Bouguer gravity map (Fig. 2), which contains several first- and second-order features that are thought to represent intra-crustal density variations that should have an expression in seismic velocities.

2 TECTONIC SETTING

The east AFO in Western Australia represents an area of extensive crustal reworking of the Archean Yilgarn Craton's southeastern margin during the Proterozoic (Myers 1990; Kirkland *et al.*
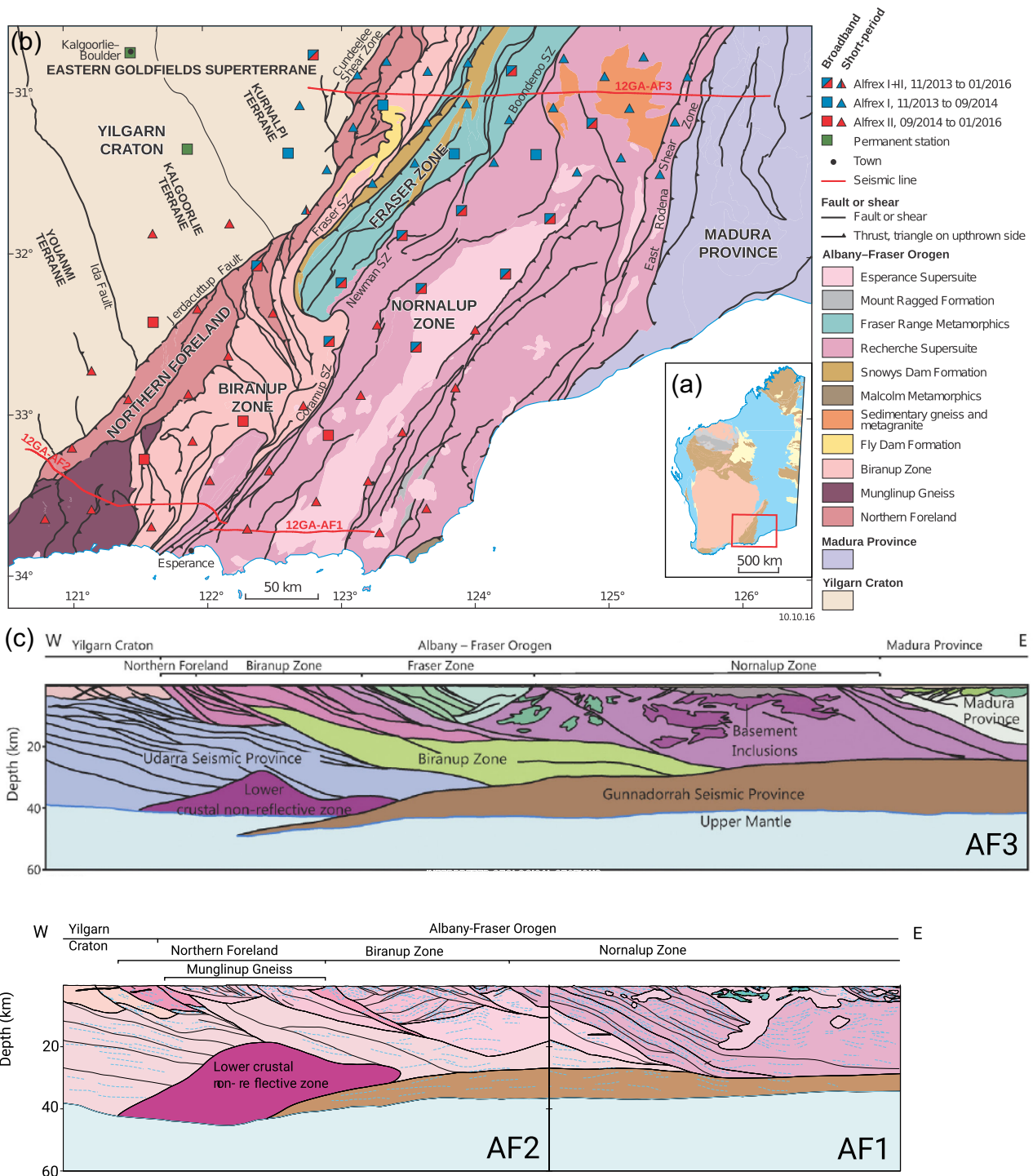
Figure 1. (a) Overview tectonic units map of Western Australia, with Archean cratons displayed in light red, Proterozoic orogens in brown and Proterozoic basins in grey and yellow. Younger surface units are shown in blue (modified after Cawood & Korsch 2008). The red frame outlines the area shown in panel (b). (b) ALFREX station deployment overlain on a simplified regional geology map of the east Albany-Fraser Orogen and its immediate surroundings. Seismic stations are displayed as triangles (short-period stations) and squares (broad-band), the colours blue and red refer to the first (November 2013–September 2014) and second (September 2014–January 2016) installation period. Regional permanent stations are shown in green, and the 2012 deep seismic reflection profiles are displayed as red lines. (c) Geological interpretation of active seismic lines 12GA-AF1 to -AF3 (positions shown in panel (b)). Figure modified after Spaggiari *et al.* (2014b).

2011; Spaggiari *et al.* 2014a, 2015). Palaeoproterozoic tectonism was dominated by extension, whereas Mesoproterozoic tectonism occurred in two stages between 1330–1280 Ma and 1225–1140 Ma (Clark *et al.* 2000; Kirkland *et al.* 2011; Spaggiari *et al.* 2015).

Stage I was triggered by arc accretion to the east in the Madura Province, and Stage II was an intracratonic reactivation event (Kirkland *et al.* 2011; Smithies *et al.* 2015). The east AFO is subdivided into the Northern Foreland and Kepa Kurl Booya Province, which
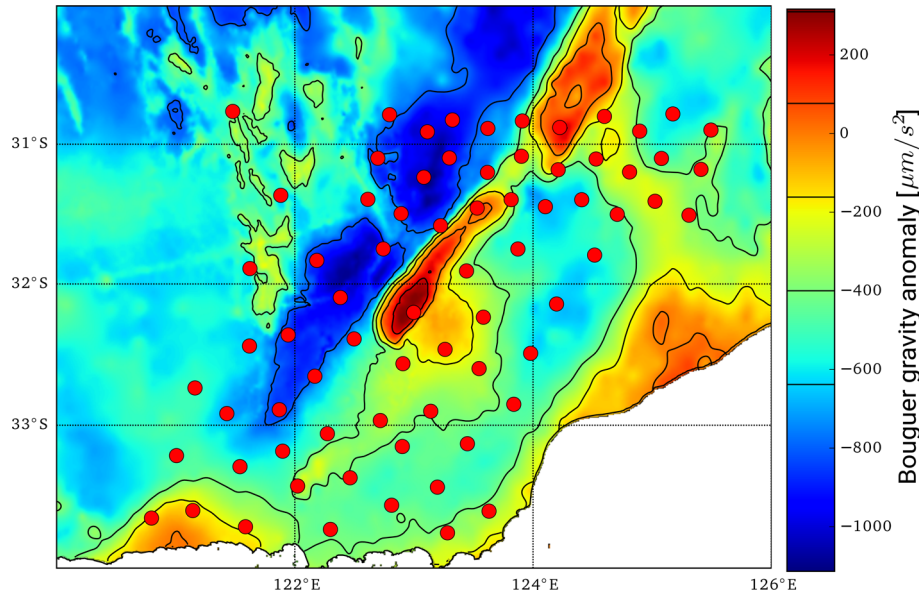
Figure 2. Regional Bouguer gravity anomaly map of the study area, showing the two parallel anomalies of opposite sign mentioned in the text. Locations of seismic stations are shown with red circles. The contour lines displayed here correspond to the contour lines overlain onto the group and phase velocity maps in Fig. 8 and Supporting Information Figs S4–S7.

is further divided into the Tropicana, Biranup, Nornalup and Fraser Zones (Fig. 1; Spaggiari *et al.* 2014a). The Northern Foreland is for the most part Archean Yilgarn Craton that was last modified during the AFO. In the east AFO it forms a narrow belt between the unmodified Yilgarn Craton and the Kepa Kurl Booya Province. East of the Northern Foreland, the Biranup Zone extends along the entire length of the AFO, comprising mainly orthogneissic rocks with ages of 1810–1625 Ma (Kirkland *et al.* 2011; Spaggiari *et al.* 2014a). The eastern Nornalup Zone consists of similar lithologies, but has been more heavily intruded by the granites of the *ca.* 1330–1280 Ma Recherche and *ca.* 1200–1140 Ma Esperance Supersuites. In its northeastern part, these rocks are overlain by the Eocene limestone successions of the Eucla Basin. In the south, the Newman and Coramup Shear Zones separate the Biranup and Nornalup Zones, but farther north they are separated by the Fraser Zone, an approximately 450 km long, northeasterly trending belt of high-density, metagabbroic granulite facies rocks (Fig. 1) that produce a prominent high in the regional Bouguer gravity map (Fig. 2). Bound by the Fraser Shear Zone to the west and south and by the Newman and Boonderoo Shear Zones to the east, this body of mafic to locally ultramafic rocks and coeval metagranitic rocks was exhumed from lower- to mid-crustal depths in the later part of Stage I of the AFO (Clark *et al.* 2014; Spaggiari *et al.* 2015; Maier *et al.* 2016). To the far east, just beyond the easternmost extent of our seismometer deployment, the Rodona Shear Zone separates the AFO from the adjacent Madura Province.

3 DATA

We used data from the temporary ALFREX deployment (Sippl *et al.* 2015), a 70-station array that was deployed in the AFO between November 2013 and January 2016. The network consisted of both short-period (1 Hz corner frequency) and broad-band sensors (Fig. 1) and was run in two periods of approximately 1 yr deployment time each. ALFREX covered all lithotectonic units from the Neoarchean Yilgarn Craton in the west to the eastern Nornalup

Zone in the east, and was complemented by two permanent stations (KMBL, AUKAL) at its northwestern edge. 12 stations were operated for the entire period of 2 yr, providing ray-path connectivity between the two sub-networks (Supporting Information Fig. S3).

4 METHOD

We retrieved empirical Green's functions for fundamental mode Rayleigh waves from cross-correlations of vertical-component traces of ambient seismic noise using all possible station pair combinations in our data set. Hourly data segments were demeaned and detrended, the instrument response was removed, traces were downsampled from 50 to 10 Hz and bandpass filtered to between 0.01 and 1 Hz before correlation. Amplitudes were normalized by multiplying with the inverse of a moving-window amplitude average (Bensen *et al.* 2007), and spectral whitening was applied. The cross correlation was performed with a time domain routine within the ObsPy software package (Beyreuther *et al.* 2010), hourly correlograms were stacked for the entire available time period. Examples of retrieved empirical Green's functions (EGFs) are shown in Fig. 3. Since we have many short-period instruments in the data set, we restricted the used period range to 2–20 s. Correlograms for short-period stations at the longest periods have lower signal-to-noise ratios (SNRs) compared to the broad-band stations, but are frequently still utilizable. Group velocities were determined using frequency-time analysis (FTAN, e.g. Levshin *et al.* 1992) and a phase-matched filtering approach (Levshin & Ritzwoller 2001; Arroucau *et al.* 2010; Young *et al.* 2011) on the envelope of the symmetric component (averaged causal and acausal parts) of the empirical Green's functions. Only cross-correlograms between stations with a spatial separation larger than 3 wavelengths were used for the retrieval of dispersion curves (e.g. Bensen *et al.* 2008; Lin *et al.* 2008), and traces with an SNR lower than 4 were discarded. This rather low choice of SNR was necessary to have sufficient paths available at the longer periods. Group velocities were determined twice, once without and once with the phase-matched filtering, and
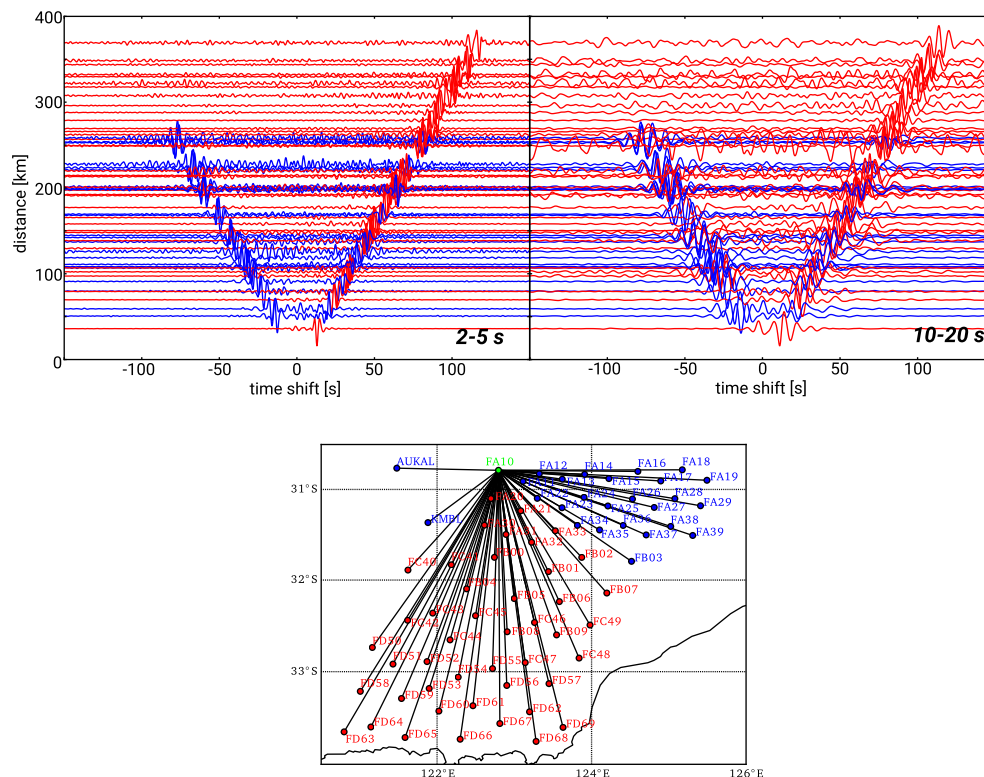
Figure 3. Example of noise cross-correlations between station FA10 and all other stations (see map in the bottom panel) for two different period bands (2–5 s and 10–20 s). Although the majority of utilized stations had short-period sensors, reasonably good signal-to-noise ratio could be achieved down to periods of 20 s. Nearly all acquired cross-correlation traces are asymmetric, with stations from southern directions showing the stronger signal in the causal branch (red traces and red labels in the map), corresponding to a predominance of noise sources in the south. Station pairs with ray paths oriented more in east-west direction (blue traces and labels) show stronger signal in the anticausal branch of the cross-correlations, which corresponds to noise sources located to the west. In both cases, the proximity to the ocean can explain the observed trend, since the study area is situated in the southwestern corner of the Australian continent (see Fig. 1a).

only measurements that were consistent between the two approaches were kept. All selected group velocity dispersion curves are shown in Fig. S1 in the Supporting Information.

For determining phase velocities, we relied on a semi-automated approach (modified from Arroucau *et al.* 2010; Young *et al.* 2011) that picks phase velocity dispersion curves from plots of phase velocity against period (after Yao *et al.* 2006). We first carefully handpicked an average dispersion curve, based on which a corridor of 'sensible' velocities was established. Dispersion curves from all station pairs were then picked automatically, whereby the resulting velocity was required to lie in the aforementioned corridor. All thus determined curves were visually checked and modified if necessary. If several branches were clearly visible in the matrix plot of phase velocity against period, we picked the slowest one that featured increasing phase velocities with period. A plot of all selected phase velocity dispersion curves is provided in Supporting Information Fig. S1.

Examples for single group and phase velocity dispersion curve picks are shown in Fig. 4. The distribution of phase and group velocities across our network is summarized as a median dispersion curve in Fig. 5. The wavelength criterion applied to the phase and group velocity determination means that the largest numbers of picks were obtained for the shorter periods between 4 and 7 s (Fig. 6), and path coverage significantly decreases for the longer periods (Supporting Information Fig. S3). The median dispersion curves hint at

overall high to very high surface wave velocities. We inverted for 2-D distributions of group and phase velocity at periods between 2 and 20 s, using the iterative nonlinear code `fmst` which employs a fast-marching method for the forward calculations (Rawlinson & Kennett 2004; Rawlinson & Sambridge 2005) and a subspace method (e.g. Kennett *et al.* 1988) for the actual inversion of surface wave velocities. The study area was parameterized as a regular grid of 60*60 nodes, which corresponds to grid cell sizes close to 10 km in both latitudinal and longitudinal direction. The tomographic inversion was performed with a total of 10 iterations, using a homogeneous starting model set to the mean velocity of all travel times at each period. After each iteration, theoretical traveltimes were recomputed. Optimal values for smoothing and damping were chosen by analysing L-curves between data and model variance (after Eberhart-Phillips 1986). Achieved variance reductions compared to the homogeneous starting model ranged between 89 and 38 per cent for phase velocities and between 85 and 20 per cent for group velocities, with the latter featuring substantially lower numbers at the longest periods (see Fig. 6). This is due both to a lower number of ray paths and a higher uncertainty in the group velocity picks at long periods (especially at 12 and 14 s; see Fig. 5 and Supporting Information Fig. S1) compared to the phase velocity ones (Fig. 4). A summary plot of the residual distributions before and after inversion is provided in Fig. 7.
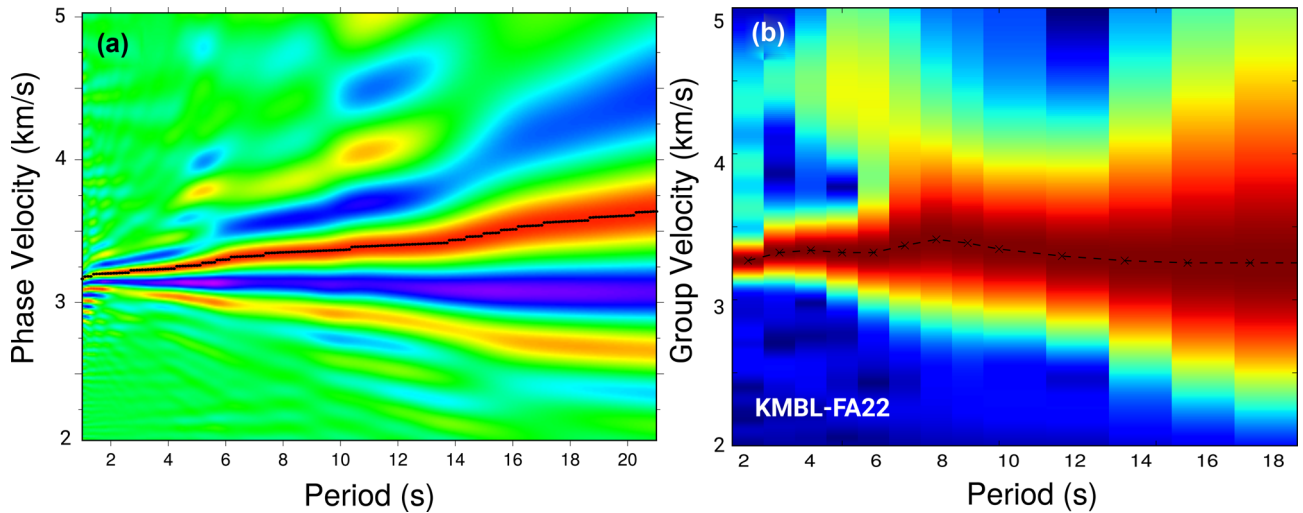
Figure 4. Examples for phase (a) and group velocity (b) determination. EGFs or their envelopes (in panel b) are plotted against period, and maximum positive amplitudes (red in both plots) are picked.
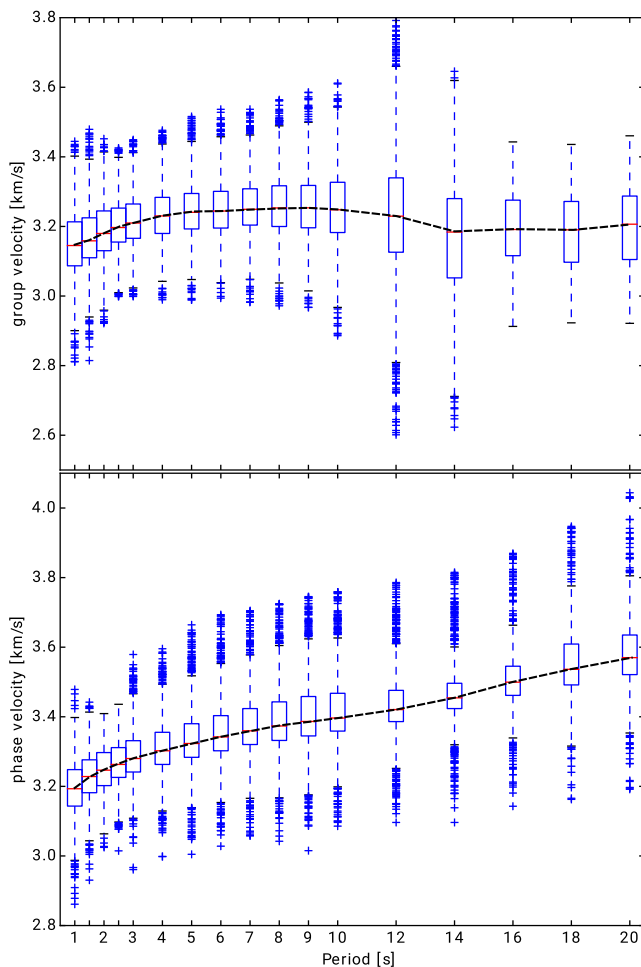

Figure 5. Median dispersion curves for group velocities (upper panel) and phase velocities (lower panel) for the entire ALFREX array. For every period, a boxplot of the distribution of retrieved velocities is shown. The black dashed line connects the median values (red horizontal lines in the boxplots) for the different periods.
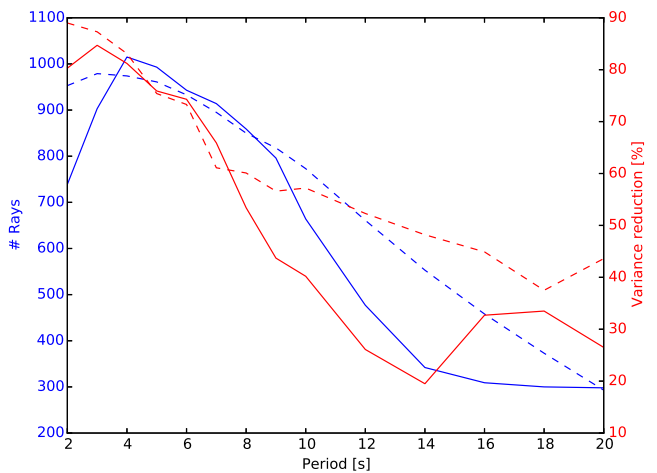

Figure 6. Plot of achieved variance reduction (red) and the number of station pairs used (blue) for group velocity (solid lines) and phase velocity (dashed lines) inversion at different periods. The number of usable station combinations decreases with period due to the wavelength criterion, which, together with higher uncertainties in the traveltime picks (see Fig. 4) leads to lower variance reductions. Phase velocity inversions perform better than group velocity inversions at longer periods.

5 RESOLUTION TESTS

Results for checkerboard resolution tests for the retrieval of phase and group velocity maps at 2, 5, 10 and 20 s period are shown in Supporting Information Fig. S2. We used the same event-station geometry, inversion settings and damping/smoothing combination as for the real data, with input anomalies of ±7.5 per cent super-imposed onto the mean velocity at each period. Input anomalies measured 2 × 2 nodes (corresponding to about 20 × 20 km), with one neutral node between anomalies of opposite sign. Gaussian noise with a standard deviation of 0.5 s (for 2 and 5 s period), 0.7 s (for 10 s period) or 1.0 s (for 20 s period) was added to the synthetic travel times to simulate the uncertainty in retriev-ing the correct phase and group velocities. The retrieved images show a noticeable reduction in resolution at the period of 20 s, where diagonal smearing of anomalies and the coalescence of single
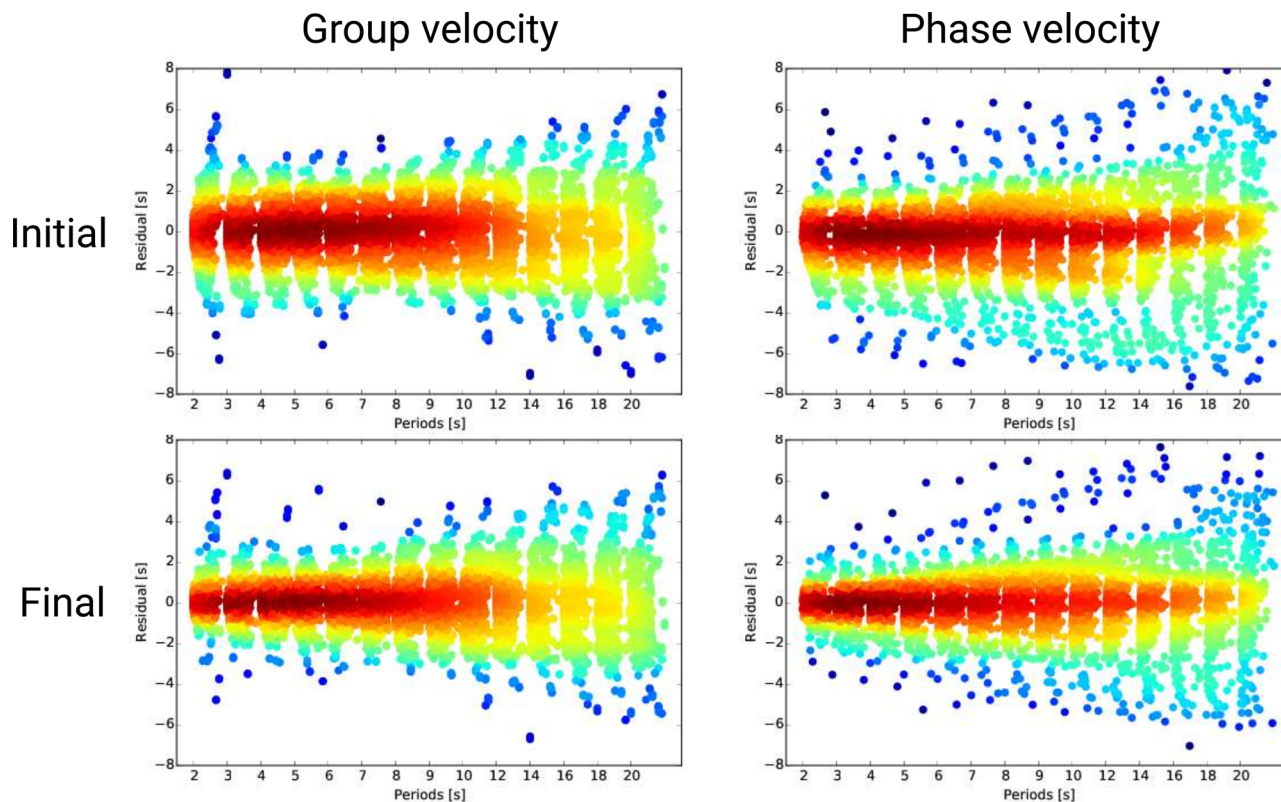
Group velocity   Phase velocity

Figure 7. Initial (upper row) and final (lower row) residual distributions for group (left column) and phase velocity (right column) inversions. For every period, traveltime residuals are plotted against traveltimes, colour coding of points is according to point density. It is apparent that while the residual distribution is significantly narrowed down for short periods, the effect is smaller for the longer periods.

vertices can be observed. This is mostly due to the substantially lower number of rays that were inverted at this period. At shorter periods, the input anomalies are reasonably well recovered over most of the study area, although with somewhat reduced amplitudes. The results from the group velocity inversion appear to be better resolved than the phase velocity images. The main reason for this is that the L-curve analysis yielded higher optimal damping values for the phase velocities at shorter periods, which was likely to be due to more scatter in the picks (see Supporting Information Fig. S1). At the northwestern edge of the network, the available resolution is consistently low, due to ray-path coverage to and from a single station only (see Supporting Information Fig. S3). Therefore anomalies retrieved in this region have been omitted from the interpretations.

6 GROUP AND PHASE VELOCITY MAPS

Group and phase velocity maps for periods of 2, 5, 10 and 20 s are shown in Fig. 8, maps for other periods can be found in the Supporting Information (Figs S4–S7). All phase and group velocity maps feature quite high average velocities clearly in excess of 3 km s^{-1} even for the shortest period of 2 s. These results confirm the anomalously high group velocities at short periods for most of Western Australia found by Saygin & Kennett (2012). Whereas phase velocities increase with period, the average group velocity dispersion curve is nearly flat (Fig. 5). The main features in the group and phase velocity maps are highly consistent, although there are differences in detail; this attests to the robustness of the retrieved velocity distributions.

The most prominent anomaly is a pronounced elongated velocity high, trending NNE in the northern half of the array (anomaly H1 in Fig. 8), which is spatially coincident with a regional gravity high (shown with orange contour lines in Fig. 8). While this anomaly can be traced from the southern end of the gravity high up to the northern end of the array in the 2 and 5 s maps, its northern part fades out in the 10 s phase velocity map, but is still clearly observed in the group velocities. At 20 s period, the anomaly is no longer visible. In most of the group and phase velocity maps, this high-velocity anomaly protrudes westward into the adjacent gravity low (H2). In the eastern and northeastern part of the array, where the Nornalup Zone is overlain by the limestones of the Eucla Basin, consistently low velocities are retrieved at short (L1) and the longest periods (L3), whereas velocities between those (i.e. at 10 s) are fast to intermediate. In the southern and western part of the study area, retrieved velocities usually do not deviate far from the mean for each period. In the far southeast of the array, an area of consistently low velocities in the vicinity of Cape Arid (L2) is imaged at all periods. The prominent high-velocity anomaly in the northwest in the 20 s phase velocity map (H3) lies in a region of low resolution (Supporting Information Fig. S2) and poor ray coverage (Supporting Information Fig. S3) and is therefore not robust.

7 DEPTH INVERSIONS

In order to better understand at which depths the imaged anomalies originate, we calculated sensitivity kernels for phase and group velocities (Fig. 9) and carried out depth inversions of dispersion curves for 6 characteristic locations (Fig. 10). Fig. 9 shows sensitivity kernels for phase and group velocities at the periods displayed
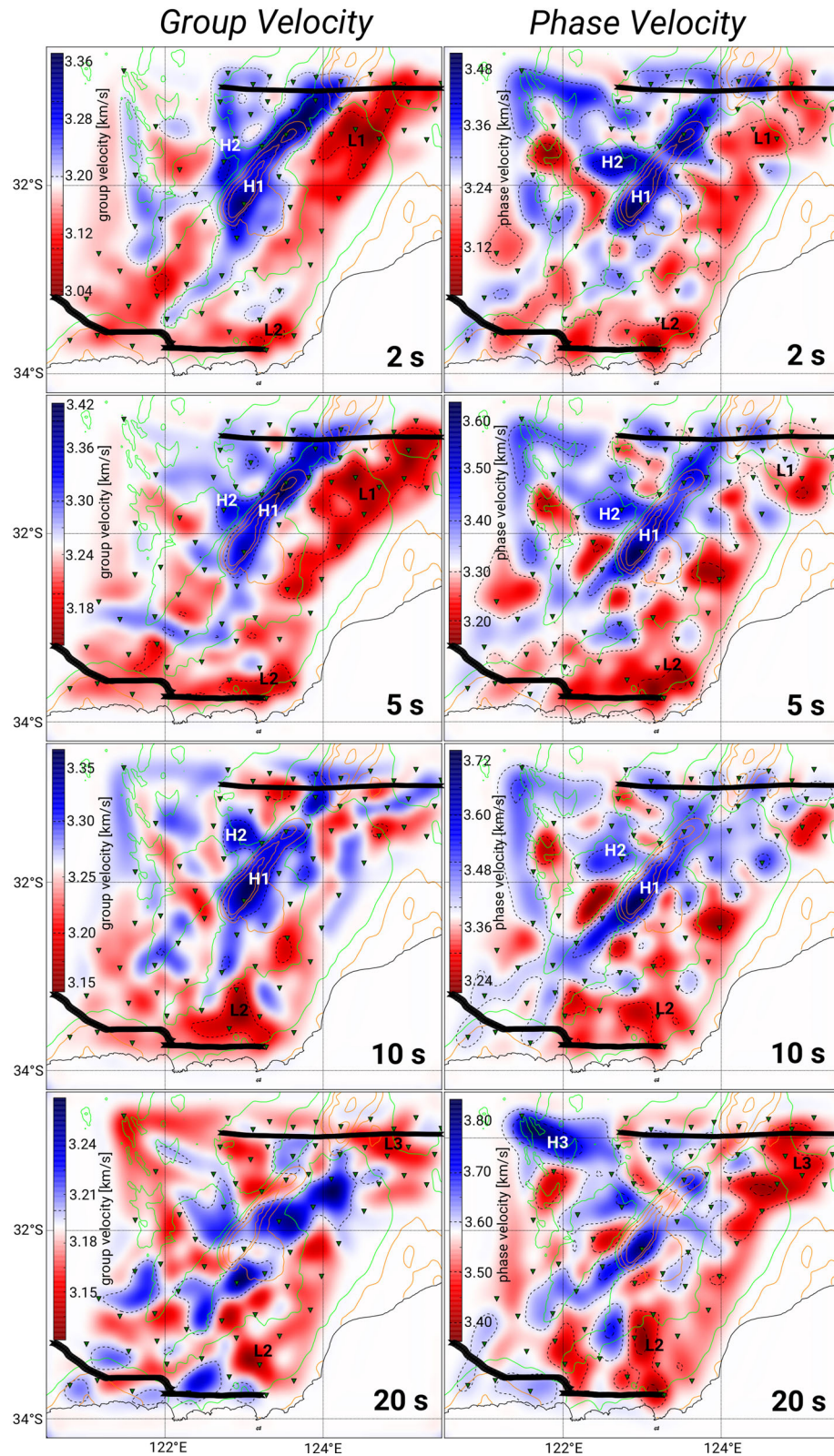
Figure 8. Group velocity maps (left column) and phase velocity maps (right column) for periods of 2, 5, 10 and 20 s. The Bouguer gravity contours are overlain in orange (positive anomalies) and green (negative anomalies). The velocity colour scales are normalized so that the mean velocity in each image appears in white, and black dashed isolines are shown every 0.1 km s^{-1}. The inverted green triangles represent the seismic stations we used, thick black lines mark the location of the 2012 deep seismic reflection profiles. Ray-path coverage for each of these maps is shown in Supporting Information Fig. S3. High- and low-velocity anomalies discussed in the text are numbered.
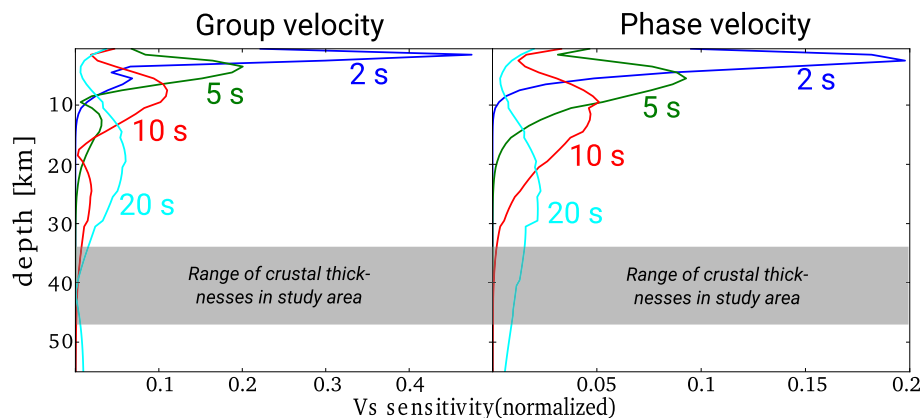
Figure 9. Sensitivity kernels for group (left) and phase velocities (right), computed using the code from Herrmann (2013) and assuming a 1-D velocity model that represents the regional average over the study area, taken from the continent-wide AusREM model (Salmon *et al.* 2013). Range of Moho depths in the study area is taken from Sippl *et al.* (2017).
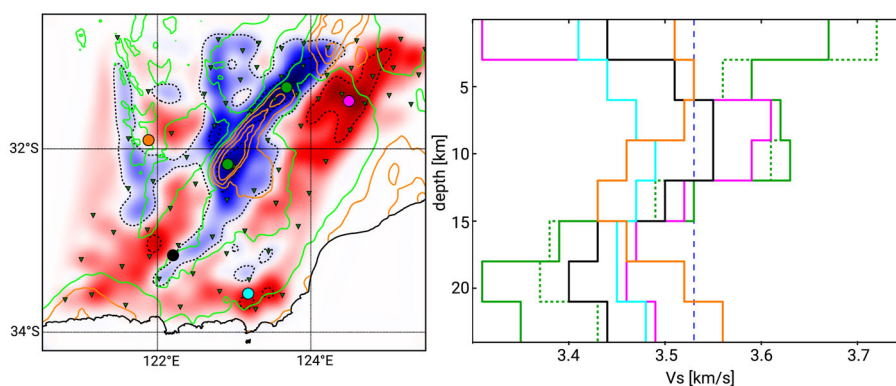

Figure 10. Left: location of the six group velocity dispersion curves (shown with coloured dots) that were inverted for 1-D shear velocity profiles, plotted on top of the group velocity map at 2 s period. Right: retrieved 1-D shear wave velocity profiles. The colour of the profile curves corresponds to the colour of the dots in the left panel; the dashed green curve corresponds to the northern one of the two dots in the Fraser Zone high velocity anomaly, the solid line to the southern one. The vertical dashed blue line marks the velocity of the homogeneous starting model.

in Fig. 8, computed using the codes of Herrmann (2013) and a regional average over the AusREM velocity model (Salmon *et al.* 2013) as background. Tests showed that the kernels only weakly depend on the utilized background velocity model, a computation using a global model yielded highly similar results. These sensitivity kernels show that the period range that we analysed is mainly sampling the upper and middle crust, with only a weak contribution from lower crustal depths at the longest periods. The influence of subcrustal regions and thus Moho topography is nearly non-existent for group velocities, and small for the phase velocities. As expected, group velocities generally sample somewhat shallower depths than phase velocities for the same period.

We inverted group velocity dispersion curves picked at six characteristic grid node points throughout the study area for 1-D v_s profiles (similar to, e.g. Domingues *et al.* 2016, see Fig. 10). The applied 1-D inversion scheme is a linearized, damped least-squares approach (Herrmann 2013), with which we performed a total of 12 iterations. After these, the changes in the resulting v_s models were minimal. The starting model was homogeneous, with $v_s = 3.53$ km s^{-1} in 8 layers of 3 km thickness each. At depths larger than 24 km, v_s was kept fixed at the same value. We applied this strategy because of the limited resolution of our data set at lower crustal and sub-crustal depths, due to the limited range of utilized periods (see Fig. 9). The retrieved v_s profiles show pronounced differences be-

tween the various regions: both points taken within the Fraser Zone (green), for instance, feature high shear wave speeds in the uppermost 12–15 km, underlain by significantly slower material. The 1-D profile located in the Eucla Basin, on the other hand, exhibits a very slow uppermost layer, but rather high velocities in the deeper part of the upper crust (magenta curve). Nearly all profiles show a decrease in shear wave velocities towards middle crustal depths.

8 DISCUSSION

We find no clear signature of the transition between Archean Yilgarn Craton and the Proterozoic AFO in our phase and group velocity maps. The maps are instead dominated by anomalies that represent more regional geological features that will be discussed in the following. Previous knowledge of the regional crustal structure comes predominantly from three active seismic lines (12GA-AF1, 12GA-AF2 and 12GA-AF3) acquired in 2012 (Fig. 1; Spaggiari *et al.* 2014b), as well as from surface geological constraints. We thus first interpret the obtained results based on these two data sets, and attempt to use the phase and group velocity maps to derive the distribution of units between the seismic profiles. In a second step, we compare the obtained anomalies to the regional Bouguer gravity map, which allows the placement of depth constraints on some of the gravity anomalies.

8.1 Interpretation of retrieved anomalies

Anomaly H1, the most prominent high-velocity anomaly we image, is clearly associated with the Fraser Zone (see Fig. 1), which is in part defined by its distinct regional high in Bouguer gravity maps (Fig. 2). The metagabbroic rocks that dominate the Fraser Zone have very high rock densities, thus creating a positive surface wave anomaly, even in the presence of locally elevated v_p/v_s ratio (Sippl *et al.* 2017). In active seismic line 12GA-AF3, which crosses the Fraser Zone in the northernmost part of our array, the Fraser Zone is imaged as a V-shaped entity (Fig. 1c) interpreted as a pop-up structure with a maximum depth of 4.2 s two-way traveltime (TWT), approximating 13 km depth (based on a conversion velocity of 6 km s^{-1}; Spaggiari *et al.* 2014b). In the phase and group velocity maps, the high-velocity anomaly associated with the Fraser Zone extends to longer periods in its southern part compared to the location where the active seismic profile crosses (central part of the Fraser Zone; Fig. 8). This is in accordance with the higher amplitudes of the gravity high in the southernmost part of the Fraser Zone, and may provide insight into the geometrical configuration of the Fraser Zone rocks and their exhumation. Alternatively, the Fraser Zone may simply be thicker in this region, regardless of the exhumation mechanism, as there are no significant differences in the observed geological relationships between its central and southern portions, that is, there is nothing to suggest a different crustal level is exposed (Maier *et al.* 2016). However, the two 1-D v_s profiles located in the northeastern and southwestern part of the Fraser Zone (Fig. 10) both show anomalously fast velocities confined to the uppermost 12–15 km, underlain by significantly slower material. No clear difference in depth extent of the elevated velocities is discernible.

The most prominent low-velocity anomaly we image (L1) is situated at shallow crustal levels throughout the eastern Nornalup Zone, approximately where the eastern Nornalup Zone is overlain by the Eocene sedimentary rocks of the Eucla Basin. Drillcores from boreholes to the east, where the basin is expected to be deeper, showed that the basement is reached at depths around 400–500 m there (Spaggiari & Smithies 2015), and a recent study by Scheib *et al.* (2016) retrieved depths to basement of ≤300 m for the part of the Eucla Basin that is situated in our study area. Thus, the fact that we still see consistently slow velocities at 5 s period most likely implies a slow uppermost basement in addition to the overlying sediments. The 1-D v_s profile for the Eucla Basin (Fig. 10; magenta curve) shows a very slow uppermost layer, and faster velocities from 6 km downwards. Information on the nature of the basement beneath the Eucla Basin is very sparse, including that beneath the northeastern Nornalup Zone. Potential field and sparse drillcore data suggest considerable complexity, including the presence of metasedimentary rocks intruded by dominantly granitic rocks of the Recherche and Esperance Supersuites (Murdie *et al.* 2014; Spaggiari *et al.* 2014b; Spaggiari & Smithies 2015). The transition from intermediate to fast velocities at 10 s, which most likely represent the basement, to markedly slow velocities at 20 s (L3) likely captures a vertical transition in the middle crust that has not been previously recognized. Such a transition may, at least in part, explain significant areas of reflectivity that are mostly restricted to the upper crust in the area near L1 in the active seismic line 12GA-AF3. These areas of reflectivity were interpreted as metasedimentary rocks in the uppermost crust, underlain by inclusions of basement within younger granites (Spaggiari *et al.* 2014b). The low-velocity anomaly beneath the Cape Arid region (L2) in the very southeast of the array is enigmatic. While the region shows a local minimum of crustal

thickness (Sippl *et al.* 2017), the active seismic profile 12GA-AF1 only extends as far as the western edge of this anomaly (Spaggiari *et al.* 2014b; Waddell *et al.* 2015). However, the far eastern end of the 12GA-AF1 profile shows a change in upper and lower crustal character that might correspond to the anomalously slow velocities we image here. In the 1-D v_s profile, this region exhibits velocities slower than adjacent areas throughout the upper crust, to a depth of 15 km.

8.2 Comparison with Bouguer gravity

Directly relating a distribution of seismic velocities to density is not a straightforward task. Although empirically determined regression curves exist that yield density values depending on v_p and/or v_s (Nafe & Drake 1957; Brocher 2005), density also varies between different rock types at the same seismic velocity, which leads to scatter around those regression curves that is often significantly larger than the anomalies one seeks to explain (e.g. Barton 1986). In the east AFO, the largest and most characteristic gravity anomalies are a pair of parallel, elongated anomalies of opposite sign that follow the general strike of the orogen (Fig. 2). These have been explained as due to a regionally thickened crust (responsible for the gravity low) in combination with dense upper crustal rocks in the Fraser Zone (Sippl *et al.* 2017). While we do not resolve the crustal structure down to Moho depths here (Fig. 9), we clearly image the elevated seismic velocities of the Fraser Zone in the upper crust (anomaly H1; see above).

The two dense units in the lower crust retrieved in the gravity models in Sippl *et al.* (2017), the Gunnadorrah seismic zone that underlies the east AFO and the denser lower crustal rocks inside the Moho 'trough' imaged with receiver functions, show no signature in our velocity models. This is not surprising because they are situated at depths below of what we can expect to resolve. However, the Bouguer gravity map helps identify the origin of anomaly H2 (Fig. 8). This high-velocity anomaly extends west of the Fraser Zone gravity high, and is situated slightly south of an area where a localized, northwesterly trending gravity high intersects the otherwise continuous gravity low that parallels the western side of the Fraser Zone (see Fig. 2). This local gravity high corresponds to the location where northwesterly trending greenstone belts of the Eastern Goldfields Superterrane extend as far southeast as the Cundeelee Shear Zone (Fig. 1), with the reworked counterparts most likely dipping to the southeast beneath the shear zone (see also Spaggiari *et al.* 2014b). It is also interesting to note that some features in the Bouguer gravity map do not appear to have a signature in our velocity maps, which could imply that they have a deeper, lower crustal origin. This applies to the prominent gravity low along the orogen's strike (see above), the gravity high in the far southwest of the array which has been linked to high-density lower crustal rocks (Sippl *et al.* 2017), and to the extension of the Fraser Zone gravity high to the southeast, which has previously been modelled as originating from a mid- to lower-crustal high-density body (Brisbout 2015).

9 CONCLUSIONS

We inverted group and phase velocity wave speeds obtained from ambient noise cross-correlation of station pairs of the ALFREX passive seismic deployment (2013–2016) in the east AFO to obtain 2-D maps of phase and group velocities at periods between 2 and 20 s. Furthermore, we tried to constrain the depth extent of the

retrieved anomalies by the calculation of sensitivity kernels and by carrying out inversions for 1-D v_s profiles at characteristic positions.

The major surface wave velocity variations across the AFO do not show a sharp transition between Neoarchean and Proterozoic rocks, as one might expect from their juxtaposition shown in geological maps. Instead, surface wave velocities mainly delineate several local features and lithological units. This could be due to the fact that the AFO crust actually contains large volumes of Neoarchean material, particularly in the lower crust, that has been thermally and structurally reworked. The most prominent surface wave speed anomalies we retrieved correspond to the Fraser Zone metamorphic rocks and the limestone and sediment successions of the Eucla Basin atop the eastern Nornalup Zone. The Fraser Zone is outlined by clearly elevated seismic velocities in the upper crust, to depths of 12–15 km. The extent of elevated surface wave velocities corresponds to the area outlined by a gravity high, which is evidence for a link between rock type and velocity here. Other prominent anomalies in the eastern part of the array are indicative of the sediment cover and basement structure of the eastern Nornalup Zone. While it is not always possible to link the units from the active seismic profiles (Fig. 1c) to a distinct velocity signature, the phase and group velocity maps from ambient noise tomography have proven useful in placing depth constraints on anomalies observed in the Bouguer gravity maps, and outlining a number of regional features more clearly.

ACKNOWLEDGEMENTS

REFERENCES

Arroucau, P., Rawlinson, N. & Sambridge, M., 2010. New insight into Cainozoic sedimentary basins and Palaeozoic suture zones in southeast Australia from ambient noise surface wave tomography, *Geophys. Res. Lett.,* **37,** 1–6.

Bacchin, M.L., Milligan, P.R., Tracey, R. & Wynne, P., 2008. *Gravity Anomaly Map of the Australian Region,* 3rd edn, Geoscience Australia.

Barton, P.J., 1986. The relationship between seismic velocity and density in the continental crust—a useful constraint?, *Geophys. J. R. astr. Soc.,* **87,** 195–208.

Bensen, G.D., Ritzwoller, M.H., Barmin, M.P., Levshin, A.L., Lin, F.C., Moschetti, M.P., Shapiro, N.M. & Yang, Y., 2007. Processing seismic ambient noise data to obtain reliable broad-band surface wave dispersion measurements, *Geophys. J. Int.,* **169,** 1239–1260.

Bensen, G.D., Ritzwoller, M.H. & Shapiro, N.M., 2008. Broadband ambient noise surface wave tomography across the United States, *J. geophys. Res.,* **113,** B05306, doi:10.1029/2007JB005248.

Beyreuther, M., Barsch, R., Krischer, L., Megies, T., Behr, Y. & Wassermann, J., 2010. ObsPy: a Python toolbox for seismology, *Seismol. Res. Lett.,* **81,** 530–533.

Brisbout, L., 2015. Determining crustal architecture in the east Albany-Fraser Orogen from geological and geophysical data, Geological Survey of Western Australia Report 152, Perth, 52 pp.

Brocher, T.M., 2005. Empirical relations between elastic wavespeeds and density in the Earth's crust, *Bull. seism. Soc. Am.,* **95,** 2081–2092.

Cawood, P.A. & Korsch, R.J., 2008. Assembling Australia: Proterozoic building of a continent, *Precambrian Res.,* **166,** 1–35.

Christensen, N.I. & Mooney, W.D., 1995. Seismic velocity structure and composition of the continental crust: a global view, *J. geophys. Res.,* **100,** 9761–9788.

Clark, D.J., Hensen, B.J. & Kinny, P.D., 2000. Geochronological constraints for a two-stage history of the Albany-Fraser Orogen, Western Australia, *Precambrian Res.,* **102,** 155–183.

Clark, C., Kirkland, C.L., Spaggiari, C.V., Oorschot, C., Wingate, M.T.D. & Taylor, R.J., 2014. Proterozoic granulite formation driven by mafic magmatism: an example from the Fraser Range Metamorphics, Western Australia, *Precambrian Res.,* **240,** 1–21.

Dalton, C.A., Gaherty, J.B. & Courtier, A.M., 2011. Crustal Vs structure in northwestern Canada: imaging the Cordillera-craton transition with ambient noise tomography, *J. geophys. Res.,* **116,** 1–30.

Domingues, A., Silveira, G., Ferreira, A.M.G., Chang, S.J., Custodio, S. & Fonseca, J.F.B.D., 2016. Ambient noise tomography of the East African Rift in Mozambique, *Geophys. J. Int.,* **204,** 1565–1578.

Eberhart-Phillips, D., 1986. Three-dimensional velocity structure in northern California coast ranges from inversion of local earthquake arrival times, *Bull. seism. Soc. Am.,* **76,** 1025–1052.

Fishwick, S., Kennett, B.L.N. & Reading, A.M., 2005. Contrasts in lithospheric structure within the Australian craton—insights from surface wave tomography, *Earth planet. Sci. Lett.,* **231,** 163–176.

Herrmann, R.B., 2013. Computer programs in seismology: an evolving tool for instruction and research, *Seismol. Res. Lett.,* **84,** 1081–1088.

Kennett, B.L.N., Sambridge, M. & Williamson, P.R., 1988. Subspace methods for large inverse problems with multiple parameter classes, *Geophys. J. Int.,* **94,** 237–247.

Kennett, B.L.N., Fichtner, A., Fishwick, S. & Yoshizawa, K., 2013. Australian Seismological Reference Model (AuSREM): mantle component, *Geophys. J. Int.,* **192,** 871–887.

Kirkland, C.L. *et al.*, 2011. On the edge: U-Pb, Lu-Hf, and Sm-Nd data suggests reworking of the Yilgarn craton margin during formation of the Albany-Fraser Orogen, *Precambrian Res.,* **187,** 223–247.

Levshin, A.L. & Ritzwoller, M.H., 2001. Automated detection, extraction, and measurement of regional surface waves, *Pure appl. Geophys.,* **158**(8), 1531–1545.

Levshin, A.L., Ratnikova, L. & Berger, J., 1992. Peculiarities of surface-wave propagation across central Eurasia, *Bull. seism. Soc. Am.,* **82,** 2464–2493.

Lin, F.C., Moschetti, M.P. & Ritzwoller, M.H., 2008. Surface wave tomography of the western United States from ambient seismic noise: Rayleigh and Love wave phase velocity maps, *Geophys. J. Int.,* **173,** 281–298.

Maier, W.D. *et al.*, 2016. Petrogenesis and Ni-Cu sulphide potential of mafic-ultramafic rocks in the Mesoproterozoic Fraser Zone within the Albany-Fraser Orogen, Western Australia, *Precambrian Res.,* **281,** 27–46.

Murdie, R., Gessner, K., Occhipinti, S., Spaggiari, C.V. & Brett, J., 2014. Interpretation of gravity and magnetic data across the Albany-Fraser Orogen, in *Albany-Fraser Orogen Seismic and Magnetotelluric (MT) Workshop 2014: Extended Abstracts*. pp. 118–134, eds Spaggiari, C.V. & Tyler, I.M., Geological Survey of Western Australia, Perth, Record 2014/06.

Myers, J.S., 1990. Precambrian tectonic evolution of part of Gondwana, southwestern Australia, *Geology,* **18,** 537–540.

Nafe, J.E. & Drake, C.L., 1957. Variation with depth in shallow and deep water marine sediments of porosity, density and the velocities of compressional and shear waves, *Geophysics,* **22,** 523–552.

Rawlinson, N. & Kennett, B.L.N., 2004. Rapid estimation of relative and absolute delay times across a network by adaptive stacking, *Geophys. J. Int.,* **157,** 332–340.

Rawlinson, N. & Sambridge, M., 2005. The fast marching method: an effective tool for tomographic imaging and tracking multiple phases in complex layered media, *Explor. Geophys.,* **36,** 341–350.

Ritsema, J., Nyblade, A.A., Owens, T.J., Langston, C. & VanDecar, J.C., 1998. Upper mantle seismic velocity structure beneath Tanzania, East Africa: implications for the stability of cratonic lithosphere, *J. geophys. Res.,* **103,** 21 201–21 213.

Rudnick, R.L. & Fountain, D.M., 1995. Nature and composition of the continental crust: A lower crustal perspective, *Revi. Geophys.,* **33,** 267–309.

Salmon, M., Kennett, B.L.N. & Saygin, E., 2013. Australian Seismological Reference Model (AuSREM): crustal component, *Geophys. J. Int.,* **192,** 190–206.

Saygin, E. & Kennett, B.L.N., 2012. Crustal structure of Australia from ambient seismic noise tomography, *J. geophys. Res.,* **117,** 1–15.

Scheib, A., Morris, P., Murdie, R. & Delle Piane, C., 2016. A passive seismic approach to estimating the thickness of sedimentary cover on the Nullarbor Plain, Western Australia, *Aust. J. Earth Sci.* **63,** 583–598.

Sippl, C., Kennett, B.L.N., Tkalčič, H., Spaggiari, C.V. & Gessner, K., 2015. New constraints on the current stress field and seismic velocity structure of the eastern Yilgarn Craton from mechanisms of local earthquakes, *Aust. J. Earth Sci.,* **62,** 921–931.

Sippl, C., Brisbout, L., Spaggiari, C., Gessner, K., Tkalčić, H., Kennett, B.L.N. & Murdie, R., 2017. Crustal structure of a Proterozoic craton boundary: east Albany-Fraser Orogen, Western Australia, imaged with passive seismic and gravity anomaly data, *Precambrian Res.,* **296,** 78–92.

Smithies, R.H., Spaggiari, C.V. & Kirkland, C.L., 2015. *Building the crust of the Albany-Fraser Orogen; constraints from granite geochemistry, Technical Report*. Geological Survey of Western Australia Report 150. Perth.

Spaggiari, C.V. & Smithies, R.H., 2015. *Eucla Basement Stratigraphic Drilling Results Release Workshop: Extended Abstracts,* Geological Survey of Western Australia, Perth, Record 2015/10.

Spaggiari, C.V., Kirkland, C.L., Smithies, R.H., Occhipinti, S. & Wingate, M.T.D., 2014a. Geological framework of the Albany-Fraser Orogen, in *Albany-Fraser Orogen Seismic and Magnetotelluric (MT) Workshop 2014: Extended Abstracts,* pp. 12–27, eds Spaggiari, C.V. & Tyler, I.M., Geological Survey of Western Australia, Perth, Record 2014/06.

Spaggiari, C.V. *et al.,* 2014b. Interpretation of Albany-Fraser seismic lines 12GA-AF1, 12GA-AF2 and 12 GA-AF3: implications for crustal architecture, in *Albany-Fraser Orogen Seismic and Magnetotelluric (MT) Workshop 2014: Extended Abstracts,* pp. 28–51, eds Spaggiari, C.V. & Tyler, I.M., Geological Survey of Western Australia, Perth, Record 2014/06.

Spaggiari, C.V., Kirkland, C.L., Smithies, R.H., Wingate, M.T.D. & Belousova, E.A., 2015. Transformation of an Archean craton margin during Proterozoic basin formation and magmatism: the Albany-Fraser Orogen, Western Australia, *Precambrian Res.,* **266,** 440–466.

Waddell, P.J.A., Timms, N.E., Spaggiari, C.V., Kirkland, C.L. & Wingate, M.T.D., 2015. Analysis of the Ragged Basin, Western Australia: insights into syn-orogenic basin evolution within the Albany-Fraser Orogen, *Precambrian Res.,* **261,** 166–187.

Yao, H., Beghein, C. & van der Hilst, R., 2006. Surface wave array tomography in SE Tibet from ambient seismic noise and two-station analysis–II. Crustal and upper-mantle structure, *Geophys. J. Int.,* **173,** 205–219.

Young, M.K., Rawlinson, N., Arroucau, P., Reading, A.M. & Tkalčić, H., 2011. High-frequency ambient noise tomography of southeast Australia: new constraints on Tasmania's tectonic past, *Geophys. Res. Lett.,* **38,** 1–6.

SUPPORTING INFORMATION

Supplementary data are available at *GJI* online.

Figure S1. All selected dispersion curves for group (left) and phase velocity (right) that were used for inverting the 2D maps.

Figure S2. Checkerboard resolution tests for group and phase velocity retrieval.

Figure S3. Raypath geometries for the group and phase velocity maps shown in Fig. 8.

Figure S4. Group velocity maps for periods of 2–9 s. For plot details refer to Fig. 8.

Figure S5. Group velocity maps for periods of 10–20 s. For plot details refer to Fig. 8.

Figure S6. Phase velocity maps for periods of 2–9 s. For plot details refer to Fig. 8.

Figure S7. Phase velocity maps for periods of 10–20 s. For plot details refer to Fig. 8.

Please note: Oxford University Press is not responsible for the content or functionality of any supporting materials supplied by the authors. Any queries (other than missing material) should be directed to the corresponding author for the paper.